Heterogeneous Catalysis Hot Paper

Zitierweise: *Angew. Chem. Int. Ed.* **2020**, *59*, 20183 – 20191
Internationale Ausgabe: doi.org/10.1002/anie.202008962
Deutsche Ausgabe: doi.org/10.1002/ange.202008962

Zeolite-Encaged Pd–Mn Nanocatalysts for CO_2 Hydrogenation and Formic Acid Dehydrogenation

Qiming Sun, Benjamin W. J. Chen, Ning Wang, Qian He, Albert Chang, Chia-Min Yang, Hiroyuki Asakura, Tsunehiro Tanaka, Max J. Hülsey, Chi-Hwa Wang, Jihong Yu und Ning Yan**

Abstract: *A CO_2-mediated hydrogen storage energy cycle is a promising way to implement a hydrogen economy, but the exploration of efficient catalysts to achieve this process remains challenging. Herein, sub-nanometer Pd–Mn clusters were encaged within silicalite-1 (S-1) zeolites by a ligand-protected method under direct hydrothermal conditions. The obtained zeolite-encaged metallic nanocatalysts exhibited extraordinary catalytic activity and durability in both CO_2 hydrogenation into formate and formic acid (FA) dehydrogenation back to CO_2 and hydrogen. Thanks to the formation of ultrasmall metal clusters and the synergic effect of bimetallic components, the $PdMn_{0.6}$@S-1 catalyst afforded a formate generation rate of 2151 $mol_{formate} mol_{Pd}^{-1} h^{-1}$ at 353 K, and an initial turnover frequency of 6860 $mol_{H_2} mol_{Pd}^{-1} h^{-1}$ for CO-free FA decomposition at 333 K without any additive. Both values represent the top levels among state-of-the-art heterogeneous catalysts under similar conditions. This work demonstrates that zeolite-encaged metallic catalysts hold great promise to realize CO_2-mediated hydrogen energy cycles in the future that feature fast charge and release kinetics.*

Introduction

Hydrogen (H_2) is an environmentally friendly and high energy density fuel,[1] yet developing reliable and efficient H_2 storage systems remains a challenge.[2] Among various strategies for H_2 storage, chemical storage, especially using liquid chemicals as hydrogen carriers, offers substantial potential for large-scale practical applications.[3] Formic acid (FA, HCOOH), a nontoxic liquid with 4.4 wt% hydrogen content and excellent stability in air and aqueous solutions, is recognized as a suitable and cost-effective liquid hydrogen-storage media.[4] The stored H_2 from FA can be released via a dehydrogenation route ($HCOOH \rightarrow H_2 + CO_2$) using suitable catalysts even at room temperature.[5] Meanwhile, utilization of carbon dioxide (CO_2) as a cheap and abundant C1 source to produce value-added chemicals or/and fuels has been regarded as a potential way to help mitigate CO_2 induced global warming.[6] The hydrogenation of CO_2 to FA/formates is a potential way to realize CO_2-mediated hydrogen storage energy cycles.[7]

In recent years, various homogeneous/heterogeneous catalysts have been investigated in separate steps for FA dehydrogenation and CO_2 hydrogenation processes.[5a,c,8] However, the catalytic systems that can boost both FA dehydrogenation and CO_2 hydrogenation are rarely reported so far, and their catalytic activities are relatively low.[9] Although homogeneous catalysts possess a high catalytic activity, shortcomings, such as easy deactivation and inseparability from the catalytic system, limit their application. Heterogeneous catalysts provide promise to overcome the above-mentioned drawbacks, attracting increasing interests.[6d,8e,f] Nonetheless, the activity of heterogeneous catalysts still needs to be improved to meet practical application requirements.

The size and electronic structure of metal species are critical factors in determining the performance of heterogeneous catalysts.[10] Generally, smaller metal species possess

[*] Dr. Q. Sun
NUS Environmental Research Institute (NERI)
National University of Singapore
138602 Singapore (Singapore)
Dr. Q. Sun, M. Hülsey, Prof. C. Wang, Prof. N. Yan
Department of Chemical and Biomolecular Engineering
National University of Singapore
4 Engineering Drive 4, 117585 Singapore (Singapore)
E-Mail: ning.yan@nus.edu.sg
Dr. B. Chen
Institute of High Performance Computing, Agency for Science, Technology and Research
1 Fusionopolis Way, #16-16 Connexis, Singapore 138632 (Singapore)
Dr. N. Wang, Prof. J. Yu
State Key Laboratory of Inorganic Synthesis and Preparative Chemistry, College of Chemistry
International Center of Future Science, Jilin University
Changchun, 130012 (P. R. China)
E-Mail: jihong@jlu.edu.cn
Prof. Q. He
Department of Materials Science and Engineering
National University of Singapore
9 Engineering Drive 1, Singapore 117575 (Singapore)
Dr. A. Chang, Prof. C. Yang
Department of Chemistry, National Tsing Hua University
Hsinchu 30013 (Taiwan)
Dr. H. Asakura, Prof. T. Tanaka
Department of Molecular Engineering
Graduate School of Engineering, Kyoto University
Kyotodaigaku Katsura, Nishikyo-ku, Kyoto 615-8510 (Japan)
Supporting information and the ORCID identification number(s) for the author(s) of this article can be found under: https://doi.org/10.1002/anie.202008962.

improved catalytic activity compared with larger metal nanoparticles due to an increased number of accessible active sites. The fabrication of multi-metallic species has also been proven effective because of the optimized electronic state of active metal sites and the synergistic/cooperative effect of multi-metallic components.[11] A significant synthetic challenge is that the small metal species, especially the multi-metal nanostructures bearing a non-noble metal component, are easy to aggregate during catalytic reactions, inducing inferior stability and poor recyclability. Zeolites with ordered microporous channels and excellent thermal stability are regarded as ideal matrix for encapsulating ultrafine metal species.[12] Recently, we synthesized zeolite-encaged small Pd nanocatalysts under direct hydrothermal conditions, which exhibited high H_2 generation rate from FA dehydrogenation due to increased accessible active sites.[11a,12h] Utilizing zeolite-encaged metallic catalysts to further realize a CO_2-mediated hydrogen energy cycle is of significance toward achieving the hydrogen economy.

In this work, we demonstrated that zeolite-encaged metallic catalysts enabled the CO_2-mediated hydrogen storage and release with high efficiency (Figure 1). Sub-nanometer bimetallic Pd-Mn clusters were implanted into silicalite-1 (S-1) zeolites via a ligand-protected method by using $[Pd(en)_2]Cl_2$ (en = ethylenediamine) and (Mn-TEPA)Cl_2 (TEPA = tetraethylenepentamine) complexes as precursors under direct hydrothermal conditions. Aberration-corrected scanning transmission electron microscopy (STEM) and extended X-ray absorption fine structure (EXAFS) analyses confirmed that the sub-nanometer metal species were completely encapsulated within the zeolite matrix. Thanks to the ultrasmall metal clusters and synergistic effect between Pd and Mn components leading to the formation of electron-enriched Pd surfaces, the formate generation rate during CO_2 hydrogenation over the $PdMn_{0.6}$@S-1 catalyst reached 526 and 2151 $mol_{formate}\,mol_{Pd}^{-1}\,h^{-1}$ at 298 and 353 K ($H_2/CO_2 = 20/20$ bar, 2 mL, 1.5 M NaOH solution), respectively. For the reversed process, the dehydrogenation of FA, the $PdMn_{0.6}$@S-1 catalyst afforded extraordinary initial turnover frequency (TOF) value of 6860 $mol_{H_2}\,mol_{Pd}^{-1}\,h^{-1}$ at 333 K without any additive.

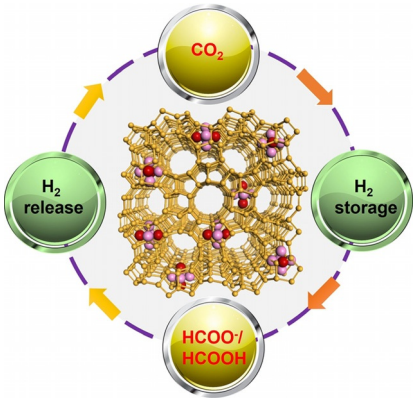

Figure 1. Schematic illustration of the CO_2-mediated hydrogen storage and release over $PdMn_x$@S-1 catalysts. The gaseous H_2 can be stored as a liquid-phase formate/formic acid with a high gravimetric and volumetric hydrogen density via the hydrogenation of CO_2. Moreover, the H_2 can be efficiently released from the decomposition of formic acid for the portable H_2 storage application. Both the hydrogen storage and release can be significantly boosted by using $PdMn_x$@S-1 nanocatalysts.

Results and Discussion

The S-1 zeolite-encaged sub-nanometer Pd-Mn clusters with different Pd/Mn molar ratios were synthesized under direct hydrothermal conditions at 170 °C for 3 days, by using $[Pd(en)_2]Cl_2$ and (Mn-TEPA)Cl_2 as metal precursors and tetrapropylammonium hydroxide (TPAOH) as template, followed by calcination in air (550 °C) and reduction in H_2 (400 °C). The molar compositions of $PdMn_x$@S-1 samples are SiO_2/TPAOH/H_2O/$[Pd(en)_2]Cl_2$/(Mn-TEPA)Cl_2 = 1/0.4/35/a/b ($a = 4.5\times10^{-3}$, $b/a = 0.2, 0.4, 0.6,$ and 0.8), where x represents the molar ratio of Mn/Pd in the initial synthesis gel. Figure 2a provides a schematic illustration of the synthetic procedure of the $PdMn_x$@S-1 catalysts. Monometallic Pd@S-1 and Mn@S-1 catalysts prepared with the same method, as well as a Pd/S-1-im sample prepared by an incipient wetness impregnation method, were used as control samples. An exothermic peak at about 350 °C in the thermogravimetric-differential thermal (TG-DTA) curves appeared in uncalcined Pd@S-1 and representative $PdMn_{0.6}$@S-1 catalysts, which was absent in the pure S-1 zeolite (Figure S1). The exothermic peak can be attributed to the oxidation of organic ligands and templates in air. The $[Pd(en)_2]Cl_2$ and (Mn-TEPA)Cl_2 complexes and TPAOH molecules remain intact during the synthesis process, as further confirmed by solid ^{13}C magic-angle spinning nuclear magnetic resonance spectroscopy (MAS NMR) (Figure S2). Powder X-ray diffraction

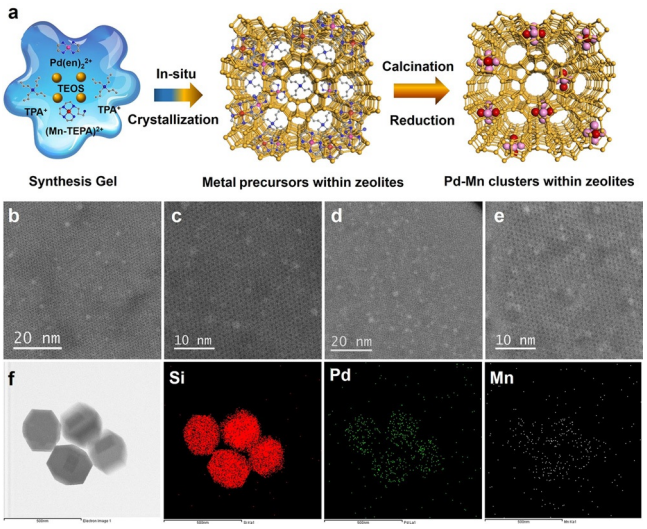

Figure 2. a) Schematic of the synthetic procedure of bimetallic $PdMn_x$@S-1 catalysts; aberration-corrected STEM-HAADF images of b,c) Pd@S-1 and d,e) $PdMn_{0.6}$@S-1 catalyst with different magnification; f) STEM image of $PdMn_{0.6}$@S-1 catalyst and the corresponding EDX mapping images for Si, Pd, and Mn elements, the scale bars of these images are 500 nm.

measurements show that the as-obtained zeolite-encaged metallic samples possess the **MFI** topological structure (Figure S3), indicating the introduction of metal species inside the zeolites hardly break the zeolite structures. No peak associated with metal species was observed, thereby ruling out the formation of bulk metal nanoparticles in the prepared materials. Inductively coupled plasma atomic emission spectroscopy (ICP-AES) measurements gave Pd loading amount of all samples within a narrow range between 0.59 to 0.63 wt %, while the Mn/Pd molar ratios of $PdMn_x$@S-1 ($x =$ 0.2, 0.4, 0.6, and 0.8) were 0.22, 0.42, 0.53, and 0.69, respectively.

TEM images of the Pd/S-1 and $PdMn_x$/S-1 catalysts are shown in Figure S4. Zeolite particles are found to be uniform in size (200–300 nm) and highly faceted, indicating good crystallinity. No metal particles were visible on the zeolite surface. Metal clusters around 1-nm or smaller were found using aberration-corrected STEM-HAADF imaging. As shown in Figure 2 b–e, while the electron beam is focused on the top-surface of the zeolite crystal to clearly show the straight channels along the *b*-axis, metal clusters appear to be blurred as they are located away from the focal point, and hence encapsulated within the zeolite structure (Figure S5).[11a,12h] Notably, the sizes of Pd clusters appear unchanged with the introduction of Mn species. Energy-dispersive X-ray (EDX) elemental mapping of representative $PdMn_{0.6}$@S-1 catalyst revealed that the Pd and Mn elements are uniformly distributed over the entire zeolite crystals (Figure 2 f). In contrast, the size distribution of Pd nanoparticles in Pd/S-1-im catalyst is uneven, giving an average size of about 3.2 nm, with most of the Pd nanoparticles located outside zeolite crystals (Figure S6). X-ray photoelectron spectroscopy (XPS) measurements show no detectable signals of Pd and Mn species over Pd@S-1, Mn@S-1 and $PdMn_x$@S-1 samples, but the peaks at 335.0 and 340.3 eV attributed to $Pd3d_{5/2}$ and $Pd3d_{3/2}$ of Pd^0 are clearly observed in Pd/S-1-im sample (Figures S7 and S8).[12h] This further confirms that the vast majority of metal species are confined within zeolite crystals in the $PdMn_x$@S-1 sample. Compared with pure S-1 zeolite, more than 90 % of microporous volumes are preserved in both Pd@S-1 and $PdMn_{0.6}$@S-1 catalysts ($\approx 0.10\ cm^3\ g^{-1}$, Figure S9 and Table S1), hinting at sufficient void space for the diffusion of reactants and products, despite the introduced metal clusters stay inside the zeolite channels.

To gain detailed electronic and structural information of metal species confined within the zeolites, X-ray absorption near-edge structure (XANES) and EXAFS spectra of Pd@S-1 and $PdMn_{0.6}$@S-1 samples were measured, and the EXAFS fitting data are summarized in Table S2. As shown in Figure 3 a, the Pd K-edge XANES spectra of Pd@S-1 and $PdMn_{0.6}$@S-1 are close to Pd foil with some differences, mainly attributable to the ultrasmall sub-nanometer sizes of metal clusters.[11a,12f] Notably, the Pd white-line intensity for $PdMn_{0.6}$@S-1 at $\approx$24369 eV is lower than that for Pd@S-1, indicating the Pd species in $PdMn_{0.6}$@S-1 possess a higher electron density than that in Pd@S-1. Apparently, the introduction of Mn species induced charge transfer from Mn to Pd and form an electron-enriched surface of Pd clusters in $PdMn_{0.6}$@S-1. The XANES spectrum of $PdMn_{0.6}$@S-1 at

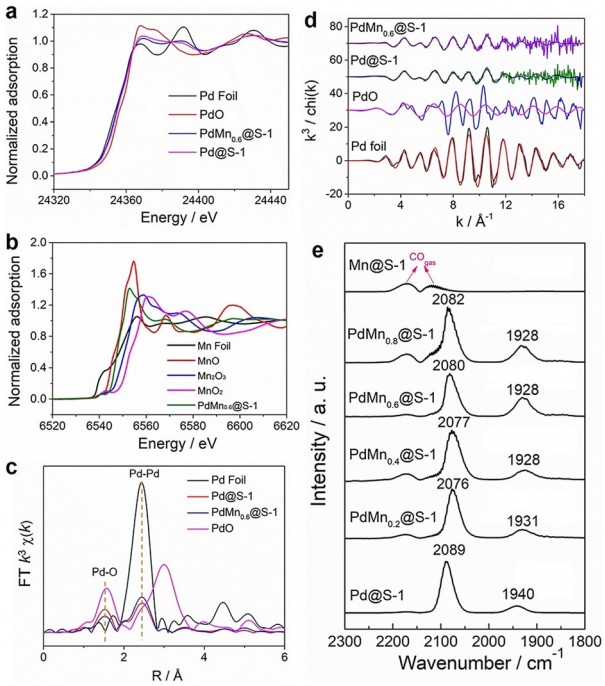

Figure 3. a) Pd K-edge XANES spectra of Pd@S-1, $PdMn_{0.6}$@S-1, Pd foil, and PdO. b) Mn K-edge XANES spectra of $PdMn_{0.6}$@S-1, Mn foil, MnO, Mn_2O_3, and MnO_2. c) Fourier transform of k^3-weighted EXAFS spectra and d) EXAFS oscillations of Pd@S-1, $PdMn_{0.6}$@S-1, Pd foil, and PdO at Pd K-edge superimposed with the fitted scattering contributions. e) In situ CO-DRIFTS measurements of Pd@S-1, Mn@S-1, and various $PdMn_x$@S-1 catalysts.

Mn K-edge is shown in Figure 3 b. The edge energy of $PdMn_{0.6}$@S-1 at Mn K-edge is between MnO and Mn_2O_3 standards, revealing that the valence of Mn species is in the range of $+2$ to $+3$. Generally, there are two forms of bonding between Pd and Mn atoms: 1) Pd-O-Mn and 2) Pd-Mn. The former one forms an electron-poor Pd species due to electron transfer from Pd to O, while the latter one forms an electron-rich Pd species due to the charge transfer from Mn to Pd. Based on the XANES results, Pd-Mn metallic bond exist and Pd-Mn alloy structures are present in $PdMn_{0.6}$@S-1, although Mn also interacts with oxygen forming MnO_x and $Mn(OH)_x$ species. The structure models of the Pd-Mn cluster in the later DFT section gives more information about the plausible structure of the Pd-Mn clusters. In the Pd K-edge Fourier-transformed EXAFS spectra (Figures 3 c and S10), the peaks at $\approx$2.00 Å and $\approx$2.73 Å attributed to Pd-O and Pd-Pd bonds, respectively, are observed in both Pd@S-1 and $PdMn_{0.6}$@S-1. The average coordination number (CN) of Pd–O bond in $PdMn_{0.6}$@S-1 is 1.7 ± 0.2, slightly lower than that in Pd@S-1 (2.0 ± 0.2 Å). The average CNs of Pd-Pd bond in Pd@S-1 and $PdMn_{0.6}$@S-1 are 3.8 ± 0.3 and 4.7 ± 0.3, respectively, suggesting that the average sizes of metal clusters in these two samples are less than 0.7 nm (corresponding to a cubo-octahedral shape with 13 atoms).[13] Although Pd-O scattering is not negligible for obtained samples, the Pd species of Pd@S-1 and $PdMn_{0.6}$@S-1 exhibit very similar oscillations to Pd foil (Figure 3 d), indicating most of the Pd in Pd@S-1 and $PdMn_{0.6}$@S-1 are metal-like species.

In situ diffuse reflectance infrared Fourier-transform spectroscopy (DRIFTS) measurements were employed to identify the electronic state of metal species in various samples, using CO molecule as a probe. As shown in Figure 3e, the peak for the linear-adsorbed CO on Pd sites shifts from 2089 cm^{-1} in Pd@S-1 to a lower wavenumber 2076–2082 cm^{-1} in $PdMn_x$@S-1. In contrast, no signal of CO adsorption was observed in Mn@S-1. In view of the similar sizes of metal clusters in Pd@S-1 and $PdMn_x$@S-1 based on STEM observations and EXAFS results, the wavenumber shift is ascribed to the electron-enriched Pd species in $PdMn_x$@S-1, in full agreement with XANES data.[8e] With the increase of Mn contents in samples, the intensity of the peak at 1928–1940 cm^{-1} attributable to the bridge-type adsorbed CO on Pd species gradually increases. It could be rationalized as the enhanced interaction between Pd and Mn species in $PdMn_x$@S-1 catalysts, which strengthens the CO adsorption on Pd sites.[14]

The thermal stability of zeolite-encaged metallic catalysts was investigated. As shown in Figures S11 and S12, the metal particle sizes of the $PdMn_{0.6}$@S-1 sample are 1.9 and 1.7 nm after calcination at 700 °C in H_2 and N_2, respectively, and no metal species is observed on the outer surface of zeolites. In contrast, the Pd nanoparticles in Pd@S-1-im are dramatically aggregated into larger particles (7.3 nm) and located on the outside of zeolites (Figure S13). Moreover, the microporous area and volume of $PdMn_{0.6}$@S-1 after calcination at 700 °C in H_2 are 146 $m^2 g^{-1}$ and 0.101 $cm^3 g^{-1}$, respectively, which are the same as those of the fresh $PdMn_{0.6}$@S-1, indicating that the zeolite structures are not destroyed. The above results demonstrate that the zeolite-encaged metallic catalysts possess remarkably improved thermal stability compared with the Pd/S-1-im counterpart. Even after five oxidation-reduction treatments at 650 °C, the metal nanoparticle size of the $PdMn_{0.6}$@S-1 sample only increases to 2.5 nm and all the metal species are still located inside the zeolite crystals (Figures S14 and 15). After thermal treatments in various atmospheres, the morphology and crystallinity of $PdMn_{0.6}$@S-1 are kept intact (Figure S16).

Figure 4a shows the catalytic activity of zeolite-encaged metallic nanocatalysts for CO_2 hydrogenation at 298 K in an H_2/CO_2 mixture (20/20 bar) using triethylamine (NEt_3) as an additive. We first measured the activity of Pd-based catalysts without Mn incorporation. As compared with the Pd/S-1-im catalyst, the Pd@S-1 catalyst exhibits near 4-fold enhancement in CO_2 hydrogenation rate. Based on the total Pd contents in the catalyst, the formate generation rate over Pd@S-1 catalyst reaches 238 $mol_{formate}\,mol_{Pd}^{-1}\,h^{-1}$, much higher than the values over commercial Pd/Al_2O_3 (53 $mol_{formate}\,mol_{Pd}^{-1}\,h^{-1}$) and Pd/C (59 $mol_{formate}\,mol_{Pd}^{-1}\,h^{-1}$) catalysts bearing Pd sizes of 2.5 and 2.1 nm, respectively (Figures S17 and S18). From H_2 pulse chemisorption measurements, the metal dispersions of Pd@S-1, Pd/C and Pd/Al_2O_3 are 94.2%, 24.5%, and 23.2%, respectively (Figure S19). Based on this, Pd@S-1 provides a TOF value of 253 h^{-1}, similar to the TOF values of Pd/C (241 h^{-1}) and Pd/Al_2O_3 (229 h^{-1}). Our previous study reveals that when the metal size is decreased to sub-nanometer and/or single-atom scale, the TOF value of CO_2 hydrogenation to formate is sharply decreased due to the formation of positively charged metal species on an oxide support.[8g] Interestingly, in this work, the sub-nanometer Pd clusters confined inside the zeolite stay in a close to a metallic state, exhibiting a similar TOF for the formate formation compared to larger Pd nanoparticles. Due to the significantly enhanced number of active sites, the Pd@S-1 catalyst offers improved formate production rate than Pd/S-1-im, Pd/C and Pd/Al_2O_3 catalysts containing larger Pd nanoparticles.

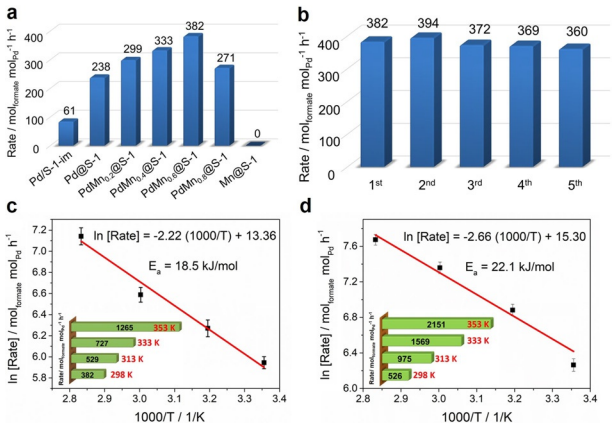

Figure 4. a) Comparison of the formate generation rates from the CO_2 hydrogenation over various catalysts and b) recycling stability tests of the $PdMn_{0.6}$@S-1 catalyst for CO_2 hydrogenation. Conditions: catalyst (5 mg), 1.5 M aqueous NEt_3 solution (2 mL), H_2/CO_2 (20/20 bar), 298 K. c) CO_2 hydrogenation over the $PdMn_{0.6}$@S-1 catalyst in the NEt_3 solution at different temperatures. Conditions: catalyst (5 mg), 1.5 M aqueous NEt_3 solution (2 mL), H_2/CO_2 (20/20 bar). d) CO_2 hydrogenation over the $PdMn_{0.6}$@S-1 catalyst in the NaOH solution at different temperatures. Conditions: catalyst (5 mg), 1.5 M aqueous NaOH solution (2 mL), H_2/CO_2 (20/20 bar).

The introduction of Mn species further enhanced the catalytic activity of CO_2 hydrogenation. The metal dispersions of $PdMn_{0.2}$@S-1, $PdMn_{0.4}$@S-1, and $PdMn_{0.6}$@S-1 are 84.7%, 84.6%, and 81.9%, respectively, comparable with that of Pd@S-1. Thus, the introduction of a small amount of Mn species does not lead to an appreciable change in the number of accessible Pd species (Figure S20). On the other hand, a substantial drop of metal dispersion to 53.8% is observed over $PdMn_{0.8}$@S-1, which is attributed to coverage of Pd atoms by enhanced amount of Mn. Among all $PdMn_x$@S-1 catalysts, $PdMn_{0.6}$@S-1 exhibited the highest formate generation rate at 382 $mol_{formate}\,mol_{Pd}^{-1}\,h^{-1}$ at 298 K corresponding to a TOF value of 466 h^{-1}. This was about 2 fold-higher than that of Pd@S-1. The Mn@S-1 catalyst without Pd is not active, suggesting Mn species only modulate the reactivity of Pd. After five consecutive runs, the formate generation rate over $PdMn_{0.6}$@S-1 catalyst remains unchanged (Figure 4b), indicating the excellent recycling stability of zeolite-encaged metallic catalysts.

Kinetic studies of $NaHCO_3$ hydrogenation over $PdMn_{0.6}$@S-1 were investigated under different concentrations of H_2 and $NaHCO_3$ at 373 K. The reaction orders of $NaHCO_3$ are 0.47 and 0.44 on the Pd@S-1 and $PdMn_{0.6}$@S-1 catalysts, respectively, whereas the orders of H_2 are 0.16 and 0.14 on these two catalysts (Figure S21). In

addition, the formate generation rate from the hydrogenation of $NaHCO_3$ was about 7-fold higher than that from the hydrogenation of Na_2CO_3 (Figure S22). From above, the formation of surface HCO_3^- appears to be the rate-determining step for the hydrogenation of CO_2 into formates. As compared with monometallic Pd@S-1 catalyst, the substantial improvement of the catalytic performance over bimetallic $PdMn_x$@S-1 catalysts can be mainly attributed to the synergistic effect between Pd and Mn species, i.e., the electron-enriched Pd surfaces have enhanced activity in formate generation, as a previous work suggested that the electron-enriched Pd species are desired in bicarbonate hydrogenation,[8e] while in situ DRIFTS measurements in the following section provide evidence that Mn promotes CO_2 transformation into bicarbonate species, which serves as a precursor for formate.

The catalytic activity increases with an increase in reaction temperature. The formate generation rate over $PdMn_{0.6}$@S-1 catalyst reached 1265 $mol_{formate}\,mol_{Pd}^{-1}\,h^{-1}$ at 353 K using NEt_3 as an additive. The apparent activation energies (E_a) of CO_2 hydrogenation to formate in the NEt_3 aqueous solution is 18.5 $kJ\,mol^{-1}$ (Figure 4c). Considering that the formate generation rates are comparable under different stirring rates (500–1400 revolutions min^{-1}), insignificant external mass transfer limitation exists in the system (Figure S23). The relatively low E_a value may be due to the compensating effects of the adsorption and desorption of substrate molecules and carbonaceous intermediates before the rate-determining step.[8b] The catalytic performance was further improved by using NaOH instead of NEt_3. The formate generation rates over $PdMn_{0.6}$@S-1 catalyst increased to 526 and 2151 $mol_{formate}\,mol_{Pd}^{-1}\,h^{-1}$ at 298 and 353 K, respectively (Figure 4d), representing the highest rates for heterogeneously catalyzed CO_2 hydrogenation into formates under similar conditions (Table S3).[8e–g,15] The E_a of CO_2 hydrogenation to formate in the NaOH aqueous solution is 22.1 $kJ\,mol^{-1}$.

To better understand the reaction mechanism for formate synthesis via CO_2 hydrogenation and the role of Mn species, in situ DRIFTS measurements were performed on Pd@S-1, $PdMn_{0.6}$@S-1, Mn@S-1, and pure S-1 catalysts. All catalysts were first activated by pure H_2 at 573 K for 1 h before the temperature decreased to 373 K and the reaction cell was purged with pure N_2 for 0.5 h. Following that, 1 bar CO_2 and H_2 (1:1) were supplied simultaneously into the reaction cell while time-resolved DRIFTS spectra were recorded over various catalysts. As shown in Figure 5a–d, the bridged carbonate (1340 cm^{-1}), monodentate bicarbonate (1680 cm^{-1}), and formate (1595, 1802–1803 and 2803–2805 cm^{-1}) species generated rapidly on Pd@S-1 and $PdMn_{0.6}$@S-1 catalysts, reaching a saturation level within 10 min.[16] Under the steady-state, the ratio of formate/bicarbonate over $PdMn_{0.6}$@S-1 catalyst is obviously higher than that of Pd@S-1 catalyst, indicating the $PdMn_{0.6}$@S-1 catalyst possesses better catalytic activity for the generation of formate via CO_2 hydrogenation than the Pd@S-1 catalyst, in accordance with activity tests. As ex-

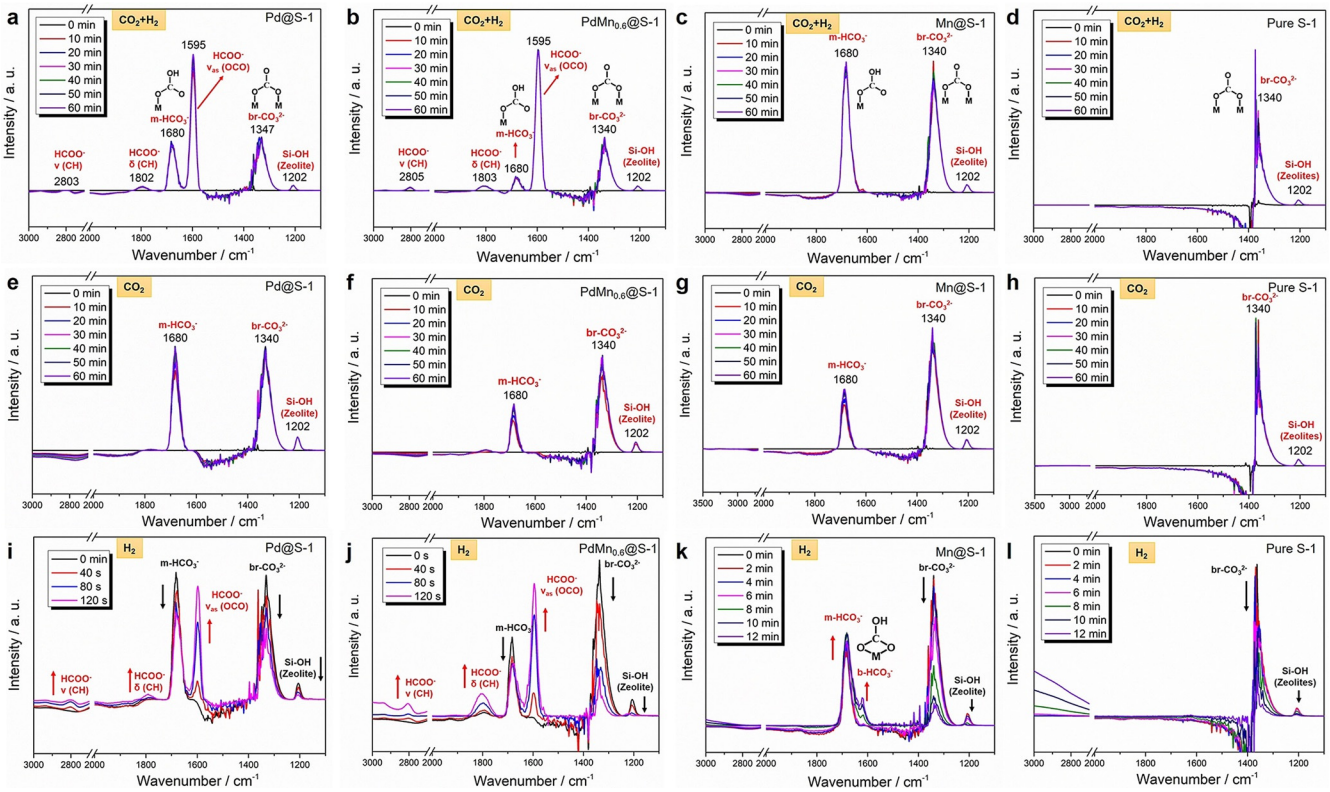

Figure 5. In situ DRIFT spectra of CO_2 hydrogenation reaction under an atmosphere of CO_2 and H_2 (1:1), and time-resolved DRIFTS spectra of first CO_2 and then H_2 stepwise reactions at 100 °C on a,e,i) Pd@S-1, b,f,j) $PdMn_{0.6}$@S-1, c,g,k) Mn@S-1, and d,h,l) pure S-1.

pected, no formate is generated on S-1 zeolite and Mn@S-1 catalysts.

Next, in situ stepwise time-resolved DRIFTS spectra of CO_2 hydrogenation were collected over various catalysts at 373 K. After activation in pure H_2 and purge with N_2, CO_2 was first introduced into the reaction cell. The bands 1340 and 1680 cm^{-1} are observed on Pd@S-1, Mn@S-1, and $PdMn_{0.6}$@S-1 catalysts, indicating the formation of bridged carbonate and monodentate bicarbonate species on the surfaces of catalysts, respectively (Figure 5e–h). However, only the bridged carbonate without monodentate bicarbonate is generated on pure S-1 zeolite. The adsorbed bicarbonate and/or carbonate species approached saturation level at 10 min. After exposure under CO_2 for 60 min, the CO_2 flow was cut off and pure H_2 was introduced into the reaction cell to investigate the reaction between H_2 and the adsorbed carbonaceous species on various catalyst surfaces. The bands at 2805, 1803, and 1595 cm^{-1} attributed to the vibrations of OCO and C–H groups in formates appear and increase gradually in the Pd@S-1 and $PdMn_{0.6}$@S-1 catalysts,[16] along with a gradual decrease of the bicarbonate and carbonate species (Figure 5i and j). In contrast, with the introduction of H_2, the bicarbonate species increase gradually along with the decrease of carbonates over the Mn@S-1 catalyst (Figure 5k); no bicarbonate and formate generate on the pure S-1 zeolite (Figure 5l). These results reveal that the adsorbed carbonaceous species are converted to formates on the Pd surfaces while the Mn species promote the conversion of carbonate to bicarbonate. It should be noticed that the increased rate of the formate/carbonate on the $PdMn_{0.6}$@S-1 catalyst is faster than that on the Pd@S-1 catalyst, indicating the introduction of Mn is conducive to the conversion of carbonate and also increase the hydrogenation ability of Pd. Based on above, we conclude that the Mn species in the $PdMn_x$@S-1 system mainly play two important roles in improving the formate generation from CO_2 hydrogenation: (1) the Mn species facilitates the formation of bicarbonates from the hydrogenation of CO_2/carbonates; (2) the introduction of Mn accelerates the hydrogenation of bicarbonates into formates over the Pd surfaces.

Catalytic activities for the hydrogen generation from FA decomposition were tested over various catalysts. As compared with the monometallic Pd@S-1 catalyst (Figure 6a), the introduction of Mn species led to remarkably improved hydrogen generation rates, among which the $PdMn_{0.6}$@S-1 catalyst showed the highest catalytic performance. 147 mL of gas ($CO_2/H_2 = 1/1$, CO < 10 ppm) was generated within 3 min at 333 K without any basic additive from 2 M FA (1.5 mL). The released gases were confirmed by gas chromatography (GC) analysis to have a CO_2 to H_2 ratio of 1:1 and was CO free (< 10 ppm) (Figure S24). Significantly, the $PdMn_{0.6}$@S-1 catalyst provided an exceptionally high initial TOF value of 6860 h^{-1} at 333 K, more than 7-fold improvement than the Pd@S-1 catalyst (944 h^{-1}). Such TOF value is among the highest level reported so far for the FA dehydrogenation without additive in heterogeneous catalytic systems under similar conditions (Table S4).[5e,f,17] Not unexpected, the Mn@S-1 catalyst exhibited no activity, confirming the Pd species are responsible for FA dehydrogenation. In

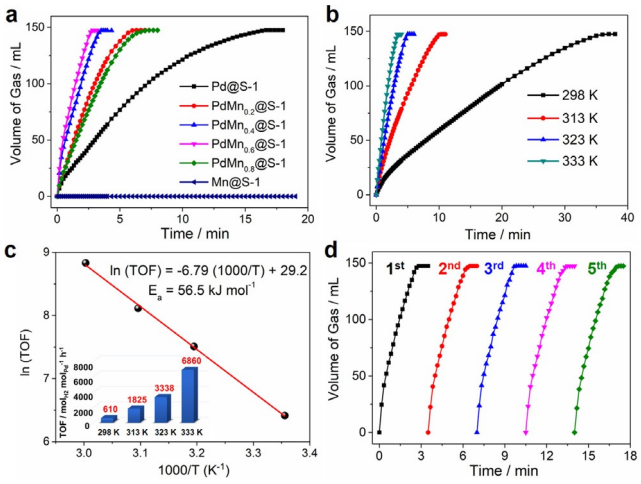

Figure 6. a) Gas generation from the FA decomposition (2.0 M, 1.5 mL) versus time over various catalysts at 333 K ($n_{Pd}/n_{FA} = 0.012$); b) Gas generation from the FA decomposition (2.0 M, 1.5 mL) versus time over $PdMn_{0.6}$@S-1 catalyst at different temperatures and c) Arrhenius plot (ln TOF vs. 1000/T) ($n_{Pd}/n_{FA} = 0.012$); d) Recycling stability tests of FA decomposition (2.0 M, 1.5 mL) over the $PdMn_{0.6}$@S-1 catalyst at 333 K.

situ DRIFTS spectra of FA dehydrogenation reactions were performed over Pd@S-1, $PdMn_{0.6}$@S-1 and Pure S-1 catalysts at 333 K. All catalysts were first activated by pure H_2 at 573 K for 1 h and then the temperature decreased to 333 K and the reaction cell was purged with pure N_2 for 0.5 h. Subsequently, the FA vapor carried by N_2 under atmospheric pressure was introduced into the reaction cell. As shown in Figure S25, after the introduction of FA vapor for 5 min, the peak at 1587 cm^{-1} assigned to vibrations of OCO of HCOO* species and peaks at 2340 and 2362 cm^{-1} assigned to gaseous CO_2 were detected on Pd@S-1 and $PdMn_{0.8}$@S-1 catalysts, but these peaks were absent on the pure S-1 catalyst. No signals of gaseous CO were detected on any sample. Therefore, the HCOO* species are the intermediate for the FA dehydrogenation while no CO byproduct is generated during the FA decomposition reactions over Pd@S-1 and $PdMn_{0.8}$@S-1 catalysts.

The H_2 generation rates accelerated along with the increase of reaction temperature. The apparent activation energy (E_a) was 56.5 kJ mol^{-1} based on the Arrhenius plot of ln(TOF) versus $1/T$, which is comparable with previously reported values.[5f,17b] In addition, the $PdMn_{0.6}$@S-1 catalyst exhibited excellent recycling stability for FA dehydrogenation. After five successive recycling tests, no decrease in catalytic activity was observed, and the morphology of zeolites and the size of ultrafine sub-nanometer metal clusters remained unchanged (Figure S26).

To rationalize the excellent catalytic performance of Pd-Mn clusters for FA decomposition in detail, first-principles density functional theory (DFT) calculations were performed. We first established the structure models of the Pd and Pd-Mn catalysts. Since the metal particle diameters are less than 0.7 nm based on EXAFS analysis, both metallic catalysts were modeled as 13-atom clusters. On the basis of theoretical studies, the most stable Pd_{13} cluster has a flat, bilayer

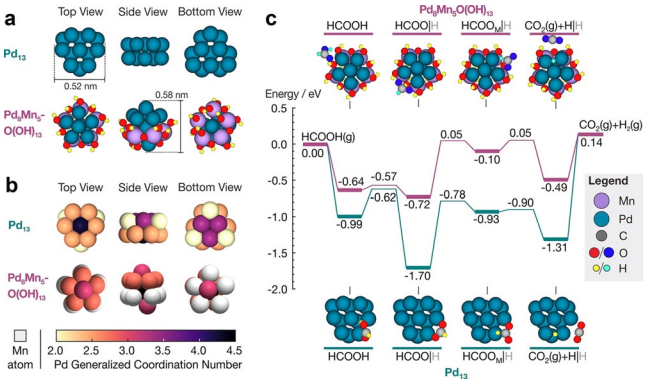

Figure 7. a) Most stable structures of Pd_{13} and $Pd_8Mn_5O(OH)_{13}$ clusters. b) Generalized coordination number of Pd atoms for the clusters. Mn atoms are shaded in white. O* and OH* species on $Pd_8Mn_5O(OH)_{13}$ are not shown for clarity. c) Potential energy diagrams for FA decomposition over Pd_{13} and $Pd_8Mn_5O(OH)_{13}$. Energies of the various states are labelled. The energies are relative to the initial state, which is gas-phase HCOOH(g) and the clean cluster. Bold lines indicate minima, whereas thin lines indicate transition states. For $Pd_8Mn_5O(OH)_{13}$, the O and H atoms of FA intermediates are highlighted in blue and cyan, respectively, for clarity. Top views of the most stable binding geometries of the various intermediates are provided. „|“ in the labels of species names denotes that energetics are evaluated at infinite separation (as opposed to coadsorption) with the spectator H species in grey font.

structure,[18] which was used as our model for the Pd catalyst (Figure 7a). To achieve a realistic model of the 13-atom Pd-Mn clusters, we focused on two main features: first, the cluster should have a composition close to $PdMn_{0.6}$; second, based on XANES results, Mn has an oxidation state between +2 and +3, suggesting that Pd-Mn catalyst is decorated with oxidizing O* and OH* species. Bearing these in mind, we combined ab initio molecular dynamics simulations to locate highly stable structures, phase diagrams to identify the ideal coverage of O* and OH* species, and Bader charge analysis to confirm the oxidation states of Mn. Ultimately, it was determined that the most plausible model that fulfilled the two requirements above was a Pd_8Mn_5 cluster decorated with 1 O* and 13 OH*, referred to herein as $Pd_8Mn_5O(OH)_{13}$ (Figure 7a). More details about how this model is reached is provided in the Methods section and Figures S27 and S28.

Next, we probed the reaction energetics of FA decomposition over both Pd_{13} and $Pd_8Mn_5O(OH)_{13}$. Out of the two main FA decomposition pathways, we only considered the formate ($HCOO^-$) pathway. The other carboxyl (COOH) pathway leads to the formation of CO,[19] which is against the experimental observations. All energetics were evaluated at infinite separation; although previous studies showed that lateral interactions between adsorbates may significantly affect the energetics of FA decomposition on small clusters,[20] coadsorption of the intermediates does not significantly impact the trends identified in our work (Figure S29). The resulting potential energy diagrams are shown in Figure 7c; energies of the studied intermediates and transition states are tabulated in Table S5. The potential energy diagram of $Pd_8Mn_5O(OH)_{13}$ (purple lines; Figure 7c) is noticeably flatter than that of Pd_{13} (green lines; Figure 7c). Pd_{13} binds HCOO* and H* over strongly, which leads to deep troughs in its potential energy surface and possible catalyst poisoning by these species. In contrast, $Pd_8Mn_5O(OH)_{13}$ binds reactants less strongly, preventing poisoning by HCOO* and H*. Analysis of the possible rate-determining steps also supports this conclusion: $Pd_8Mn_5O(OH)_{13}$ catalyzes the decomposition of HCOO* to $CO_2(g)$ + H* via the monodentate HCOO intermediate ($HCOO_M$*) with lower barriers (0.77 eV) than Pd_{13} (0.92 eV). A similar trend is also found for H_2 recombination (0.63 eV versus 1.45 eV).

There are two main reasons to explain why $Pd_8Mn_5O(OH)_{13}$ does not bind intermediates as strongly as Pd_{13}. Firstly, most of the Pd atoms in the cluster are bound to one O* or OH* (Figure 7a). This partial passivation weakens their binding of the FA decomposition intermediates according to the principle of bond order conservation. Secondly, the Pd atoms of $Pd_8Mn_5O(OH)_{13}$ are also less undercoordinated than those of Pd_{13} (Figure 7b). We quantified the degree of undercoordination with the generalized coordination number (GCN),[21] which is a coordination-number weighted sum of the number of neighbors that an atom has; a lower GCN denotes higher undercoordination. The Pd atoms of Pd_{13} have low GCNs of 2.00–4.25 due to the flat structure of Pd_{13}. In contrast, due to the more compact structure of $Pd_8Mn_5O(OH)_{13}$, its Pd atoms have higher GCNs of 2.75–5.17 and intrinsically binds HCOO* and H* weaker. Combined, the theoretical results suggest an interesting synergy between Mn and Pd, whereby Mn attracts spectator O* and OH* species, and therefore slightly passivates the Pd atoms in the Pd-Mn catalyst. Additionally, Mn appears to promote a more compact 3D structure, which decreases affinity of the Pd-Mn cluster towards species that bind on pure Pd cluster overly strongly. These two factors lead to the Pd-Mn catalyst furnishing right energetics to achieve a good balance between its ability to adsorb reactants and desorb products.

Conclusion

In summary, we have developed highly efficient heterogeneous catalysts based on zeolite-encaged metallic nanocatalysts to achieve CO_2-mediated hydrogen energy cycle. Sub-nanometer bimetallic Pd-Mn clusters were encapsulated within S-1 zeolites by using a ligand-protected method under in situ hydrothermal conditions. The obtained $PdMn_x$@S-1 catalysts exhibited excellent catalytic activity for H_2 storage and release mediated by CO_2. Due to the formation of ultrasmall and well-dispersed metal clusters and the synergic effect between the bimetallic components, both the formate generation rate from CO_2 hydrogenation and the H_2 generation rate in FA decomposition represent the top levels among the heterogeneous catalysts under similar conditions reported so far. The DFT calculations reveal that alloying of Pd with Mn favored the formation of a more compact structure, and slightly passivated Pd active sites, preventing overly strong binding with intermediates in FA decomposition. This work highlights that zeolite-encaged bimetallic catalysts are promising for the efficient CO_2-mediated H_2 cycle. Both fast charging and releasing can be

achieved over the same catalyst simply by adjusting the reaction condition.

Acknowledgements

This research is supported by the National Research Foundation (NRF), Prime Minister's Office, Singapore under its Campus for Research Excellence and Technological Enterprise (CREATE) programme (Grant Number R-706-001-102-281). Q.S. and J.Y. thank the 111 Project of China (B17020) for financial support. Computational work was partially performed with the resources of the National Supercomputing Centre, Singapore. Q.H. would like to acknowledge the support by National Research Foundation (NRF) Singapore, under its NRF Fellowship (NRF-NRFF11-2019-0002). XAS measurements were performed at public beamline, BL01B1, in SPring-8 with the approval of JASRI (Proposal Nos. 2018A1429, 2019A1398, 2019A1447). National Synchrotron Radiation Research Centre (NSRRC) of Taiwan is gratefully acknowledged for XAS measurements.

Conflict of interest

The authors declare no conflict of interest.

Stichwörter: CO_2 hydrogenation · formic acid · heterogeneous catalysis · hydrogen storage · zeolites

[1] P. P. Edwards, V. L. Kuznetsov, W. I. F. David, N. P. Brandon, *Energy Policy* **2008**, *36*, 4356 – 4362.
[2] a) L. Schlapbach, A. Zuttel, *Nature* **2001**, *414*, 353 – 358; b) J. Graetz, *Chem. Soc. Rev.* **2009**, *38*, 73 – 82.
[3] a) Q. Sun, N. Wang, Q. Xu, J. Yu, *Adv. Mater.* **2020**, *32*, 2001818; b) Q.-L. Zhu, Q. Xu, *Energy Environ. Sci.* **2015**, *8*, 478 – 512.
[4] a) M. Grasemann, G. Laurenczy, *Energy Environ. Sci.* **2012**, *5*, 8171 – 8181; b) K. Sordakis, C. Tang, L. K. Vogt, H. Junge, P. J. Dyson, M. Beller, G. Laurenczy, *Chem. Rev.* **2018**, *118*, 372 – 433; c) Z. Li, Q. Xu, *Acc. Chem. Res.* **2017**, *50*, 1449 – 1458.
[5] a) Q.-L. Zhu, N. Tsumori, Q. Xu, *Chem. Sci.* **2014**, *5*, 195 – 199; b) Z.-L. Wang, J.-M. Yan, Y. Ping, H.-L. Wang, W.-T. Zheng, Q. Jiang, *Angew. Chem. Int. Ed.* **2013**, *52*, 4406 – 4409; *Angew. Chem.* **2013**, *125*, 4502 – 4505; c) K. Jiang, K. Xu, S. Zou, W.-B. Cai, *J. Am. Chem. Soc.* **2014**, *136*, 4861 – 4864; d) J.-M. Yan, S.-J. Li, S.-S. Yi, B.-R. Wulan, W.-T. Zheng, Q. Jiang, *Adv. Mater.* **2018**, *30*, 1703038; e) W. Hong, M. Kitta, N. Tsumori, Y. Himeda, T. Autrey, Q. Xu, *J. Mater. Chem. A* **2019**, *7*, 18835 – 18839; f) A. Bulut, M. Yurderi, Y. Karatas, Z. Say, H. Kivrak, M. Kaya, M. Gulcan, E. Ozensoy, M. Zahmakiran, *ACS Catal.* **2015**, *5*, 6099 – 6110.
[6] a) W. Wang, S. Wang, X. Ma, J. Gong, *Chem. Soc. Rev.* **2011**, *40*, 3703 – 3727; b) A. Otto, T. Grube, S. Schiebahn, D. Stolten, *Energy Environ. Sci.* **2015**, *8*, 3283 – 3297; c) W.-H. Wang, Y. Himeda, J. T. Muckerman, G. F. Manbeck, E. Fujita, *Chem. Rev.* **2015**, *115*, 12936 – 12973; d) A. Álvarez, A. Bansode, A. Urakawa, A. V. Bavykina, T. A. Wezendonk, M. Makkee, J. Gascon, F. Kapteijn, *Chem. Rev.* **2017**, *117*, 9804 – 9838; e) X. Su, X.-F. Yang, Y. Huang, B. Liu, T. Zhang, *Acc. Chem. Res.* **2019**, *52*, 656 – 664.
[7] a) A. Boddien, F. Gärtner, C. Federsel, P. Sponholz, D. Mellmann, R. Jackstell, H. Junge, M. Beller, *Angew. Chem. Int. Ed.* **2011**, *50*, 6411 – 6414; *Angew. Chem.* **2011**, *123*, 6535 – 6538; b) J. F. Hull, Y. Himeda, W.-H. Wang, B. Hashiguchi, R. Periana, D. J. Szalda, J. T. Muckerman, E. Fujita, *Nat. Chem.* **2012**, *4*, 383 – 388; c) Q.-Y. Bi, J.-D. Lin, Y.-M. Liu, X.-L. Du, J.-Q. Wang, H.-Y. He, Y. Cao, *Angew. Chem. Int. Ed.* **2014**, *53*, 13583 – 13587; *Angew. Chem.* **2014**, *126*, 13801 – 13805; d) S. Enthaler, J. von Langermann, T. Schmidt, *Energy Environ. Sci.* **2010**, *3*, 1207 – 1217.
[8] a) J. Su, M. Lu, H. Lin, *Green Chem.* **2015**, *17*, 2769 – 2773; b) G. A. Filonenko, W. L. Vrijburg, E. J. M. Hensen, E. A. Pidko, *J. Catal.* **2016**, *343*, 97 – 105; c) H. Park, J. H. Lee, E. H. Kim, K. Y. Kim, Y. H. Choi, D. H. Youn, J. S. Lee, *Chem. Commun.* **2016**, *52*, 14302 – 14305; d) Q. Liu, X. Yang, L. Li, S. Miao, Y. Li, Y. Li, X. Wang, Y. Huang, T. Zhang, *Nat. Commun.* **2017**, *8*, 1407; e) K. Mori, T. Sano, H. Kobayashi, H. Yamashita, *J. Am. Chem. Soc.* **2018**, *140*, 8902 – 8909; f) Q. Sun, X. Fu, R. Si, C.-H. Wang, N. Yan, *ChemCatChem* **2019**, *11*, 5093 – 5097; g) Z. Zhang, L. Zhang, M. J. Hülsey, N. Yan, *Mol. Catal.* **2019**, *475*, 110461; h) A. Dubey, L. Nencini, R. R. Fayzullin, C. Nervi, J. R. Khusnutdinova, *ACS Catal.* **2017**, *7*, 3864 – 3868; i) M. S. Jeletic, M. T. Mock, A. M. Appel, J. C. Linehan, *J. Am. Chem. Soc.* **2013**, *135*, 11533 – 11536.
[9] a) A. Boddien, H. Junge, *Nat. Nanotechnol.* **2011**, *6*, 265 – 266; b) J. H. Lee, J. Ryu, J. Y. Kim, S.-W. Nam, J. H. Han, T.-H. Lim, S. Gautam, K. H. Chae, C. W. Yoon, *J. Mater. Chem. A* **2014**, *2*, 9490 – 9495; c) K. Mori, S. Masuda, H. Tanaka, K. Yoshizawa, M. Che, H. Yamashita, *Chem. Commun.* **2017**, *53*, 4677 – 4680.
[10] L. Liu, A. Corma, *Chem. Rev.* **2018**, *118*, 4981 – 5079.
[11] a) Q. Sun, N. Wang, Q. Bing, R. Si, J. Liu, R. Bai, P. Zhang, M. Jia, J. Yu, *Chem* **2017**, *3*, 477 – 493; b) G. Chen, Y. Zhao, G. Fu, P. N. Duchesne, L. Gu, Y. Zheng, X. Weng, M. Chen, P. Zhang, C.-W. Pao, J.-F. Lee, N. Zheng, *Science* **2014**, *344*, 495 – 499.
[12] a) J. D. Kistler, N. Chotigkrai, P. Xu, B. Enderle, P. Praserthdam, C.-Y. Chen, N. D. Browning, B. C. Gates, *Angew. Chem. Int. Ed.* **2014**, *53*, 8904 – 8907; *Angew. Chem.* **2014**, *126*, 9050 – 9053; b) L. Liu, M. Lopez-Haro, C. W. Lopes, C. Li, P. Concepcion, L. Simonelli, J. J. Calvino, A. Corma, *Nat. Mater.* **2019**, *18*, 866 – 873; c) L. Wang, S. Xu, S. He, F.-S. Xiao, *Nano Today* **2018**, *20*, 74 – 83; d) Y. Liu, Z. Li, Q. Yu, Y. Chen, Z. Chai, G. Zhao, S. Liu, W.-C. Cheong, Y. Pan, Q. Zhang, L. Gu, L. Zheng, Y. Wang, Y. Lu, D. Wang, C. Chen, Q. Peng, Y. Liu, L. Liu, J. Chen, Y. Li, *J. Am. Chem. Soc.* **2019**, *141*, 9305 – 9311; e) Q. Sun, N. Wang, R. Bai, Y. Hui, T. Zhang, D. A. Do, P. Zhang, L. Song, S. Miao, J. Yu, *Adv. Sci.* **2019**, *6*, 1802350; f) Q. Sun, N. Wang, T. Zhang, R. Bai, A. Mayoral, P. Zhang, Q. Zhang, O. Terasaki, J. Yu, *Angew. Chem. Int. Ed.* **2019**, *58*, 18570 – 18576; *Angew. Chem.* **2019**, *131*, 18743 – 18749; g) N. Wang, Q. Sun, J. Yu, *Adv. Mater.* **2019**, *31*, 1803966; h) N. Wang, Q. Sun, R. Bai, X. Li, G. Guo, J. Yu, *J. Am. Chem. Soc.* **2016**, *138*, 7484 – 7487; i) Q. Sun, N. Wang, Q. Fan, L. Zeng, A. Mayoral, S. Miao, R. Yang, Z. Jiang, W. Zhou, J. Zhang, T. Zhang, J. Xu, P. Zhang, J. Cheng, D.-C. Yang, R. Jia, L. Li, Q. Zhang, Y. Wang, O. Terasaki, J. Yu, *Angew. Chem. Int. Ed.* **2020**, https://doi.org/10.1002/anie.202003349; *Angew. Chem.* **2020**, https://doi.org/10.1002/ange.202003349.
[13] L. Liu, U. Díaz, R. Arenal, G. Agostini, P. Concepción, A. Corma, *Nat. Mater.* **2017**, *16*, 132 – 138.
[14] N. Tsubaki, S. Sun, K. Fujimoto, *J. Catal.* **2001**, *199*, 236 – 246.
[15] X. Shao, X. Yang, J. Xu, S. Liu, S. Miao, X. Liu, X. Su, H. Duan, Y. Huang, T. Zhang, *Chem* **2019**, *5*, 693 – 705.
[16] E.-M. Köck, M. Kogler, T. Bielz, B. Klötzer, S. Penner, *J. Phys. Chem. C* **2013**, *117*, 17666 – 17673.
[17] a) J.-M. Yan, Z.-L. Wang, L. Gu, S.-J. Li, H.-L. Wang, W.-T. Zheng, Q. Jiang, *Adv. Energy Mater.* **2015**, *5*, 1500107; b) A. Bulut, M. Yurderi, Y. Karatas, M. Zahmakiran, H. Kivrak, M. Gulcan, M. Kaya, *Appl. Catal. B* **2015**, *164*, 324 – 333; c) Q. Liu, X. Yang, Y. Huang, S. Xu, X. Su, X. Pan, J. Xu, A. Wang, C. Liang, X. Wang, T. Zhang, *Energy Environ. Sci.* **2015**, *8*, 3204 –

3207; d) Y. Luo, Q. Yang, W. Nie, Q. Yao, Z. Zhang, Z. Lu, *ACS Appl. Mater. Interfaces* **2020**, *12*, 8082 – 8090; e) S. Li, Y. Zhou, X. Kang, D. Liu, L. Gu, Q. Zhang, J. Yan, Q. Jiang, *Adv. Mater.* **2019**, *31*, 1806781.

[18] A. M. Köster, P. Calaminici, E. Orgaz, D. R. Roy, J. U. Reveles, S. N. Khanna, *J. Am. Chem. Soc.* **2011**, *133*, 12192 – 12196.

[19] S. Bhandari, S. Rangarajan, C. T. Maravelias, J. A. Dumesic, M. Mavrikakis, *ACS Catal.* **2020**, *10*, 4112 – 4126.

[20] B. W. J. Chen, M. Stamatakis, M. Mavrikakis, *ACS Catal.* **2019**, *9*, 9446 – 9457.

[21] F. Calle-Vallejo, J. I. Martínez, J. M. García-Lastra, P. Sautet, D. Loffreda, *Angew. Chem. Int. Ed.* **2014**, *53*, 8316 – 8319; *Angew. Chem.* **2014**, *126*, 8456 – 8459.

Manuskript erhalten: 27. Juni 2020
Veränderte Fassung erhalten: 5. August 2020
Akzeptierte Fassung online: 7. August 2020
Endgültige Fassung online: 15. September 2020

